Nanoscale mechanisms of CNT growth and etching in plasma environment

Nanoscale mechanisms of CNT growth and etching in plasma environment

Umedjon Khalilov[*1], Annemie Bogaerts[1], Shahzad Hussain[2], Eva Kovacevic[2], Pascal Brault[2], Chantal Boulmer-Leborgne[2] and Erik C. Neyts[1]

[1]*Research group PLASMANT, Department of Chemistry, University of Antwerp, Universiteitsplein 1, 2610 Wilrijk, Antwerp, Belgium*

[2]*GREMI UMR 7344 CNRS & Université d'Orléans, 45067 Orléans Cedex 2, France*

Abstract

Plasma-enhanced chemical deposition (PECVD) of carbon nanotubes has already been shown to allow chirality control to some extent. In PECVD, however, etching may occur simultaneously with the growth, and the occurrence of intermediate processes further significantly complicates the growth process.

We here employ a computational approach with experimental support to study the plasma-based formation of Ni nanoclusters, Ni-catalyzed CNT growth and subsequent etching processes, in order to understand the underpinning nanoscale mechanisms. We find that hydrogen is the dominant factor in both the re-structuring of a Ni film and the subsequent appearance of Ni nanoclusters, as well as in the CNT nucleation and etching processes. The obtained results are compared with available theoretical and experimental studies and provide a deeper understanding of the occurring nanoscale mechanisms in plasma-assisted CNT nucleation and growth.

Key-words: carbon nanotube, Ni nanocatalyst, PECVD, computer simulations, electron microscopy, H_2 plasma, hydrocarbons, etching.

Introduction

Ever since the discovery of carbon nanotubes (CNT) [1-3], obtaining control over its chirality-dependent properties has been a major topic of research. Such control is needed to allow their commercial application in full [4]. While the precise control of the obtained structure is still a daunting task, significant achievements have already been attained both experimentally and computationally [5-7].

Among other growth techniques [2, 3, 8, 9], thermal chemical vapor deposition (TCVD) and plasma enhanced chemical vapor deposition (PECVD) show several advantages [6, 10]. Especially, PECVD allows low-temperature growth, which is envisaged as a means towards chirality control and a reduced chirality distribution with respect to thermal growth [7, 11, 12]. Furthermore, plasma pre-treatment of the catalyst can greatly modify the resulting nanotubes [13, 14]. So far, however, the nature of the catalyst formation process by annealing metal thin films (such as Ni, Co or Fe) with or without plasma is not fully understood. Particularly, the reason and mechanism of the appearance of small and uniform nanoparticles in H_2 plasma is still not clear [15].

Besides the size control of the catalyst nanoparticles, several other factors are also of considerable importance, including the carbon chemical potential [16, 17], the necessity of a carbide phase [18-21], the importance of metal-mediated defect healing [22, 23], the influence of growth precursor, etc. All of these factors have been investigated to some extent, but a clear and consistent picture has not yet emerged. Also, in PECVD-based CNT growth, the role of C atoms or C_2 dimers [24] or energetic C-ions [25, 26] as input gas, as well as the influence of Ar^+ bombardment [25, 27], have been computationally studied. Nevertheless, the role of the plasma-generated growth precursor in CNT growth, and in particular the hydrocarbon C_nH_m species in the incubation stage of CNT nucleation [28], is not yet properly understood.

Under plasma conditions, the growth kinetics of CNTs can be expressed as a balance between the growth and etching processes [10]. Besides its damaging effect on a growing CNT structure, plasma-assisted etching can also be used to separate semiconductor CNTs from their metallic counterparts [29]. Overall, however, the etching onset is poorly studied during the CNT nucleation from plasma species, including H-radicals and ions. However, the ions are not direct sources in both CNT growth/etching, in contrast to the H-radical and hydrocarbon species [30].

Overall understanding of these processes, i.e., re-structuring of the metal catalyst, and CNT nucleation and subsequent etching, require a careful investigation of the intermediate processes taking place in nanoseconds, which is difficult to attain experimentally. On the other hand, simulations are typically computationally expensive if they are to address the inherent time and length scales. Nevertheless, both obstacles may be overcome by pursuing a combined modeling/experimental approach addressing the aforementioned issues. In the current contribution, we investigate both subjects by the modeling of the nanocatalyst formation and subsequent CNT nucleation/etching, and by performing experiments to obtain nanoclusters and CNT carpets in both thermal and plasma mode.

Methods

1. Simulation details

The simulated deposition of Ni atoms onto a semiconductor substrate is performed using the LAMMPS open source code [31]. In the simulations, two Si crystals with a size of 5.43 nm × 5.43 nm × 2.6 nm and 8.15 nm × 8.15 nm × 2.6 nm are used as a substrate, containing 3995 and 8888 silicon atoms, respectively. In both cases, the substrate temperature is equilibrated to 300 K, controlled by a Berendsen thermostat [32] with a damping constant of 0.1 ps. The atoms of the bottom layer are fixed. During the deposition, a Ni atom is randomly positioned at least 1 nm above the Si(100) surface every 0.5 ps : this value prevents thermal relaxation interactions between consecutive Ni impacts on the Si surface [33]. The Ni initial velocities are randomly and uniformly chosen in the range 0.05-0.3 nm/ps towards the surface. Tersoff [34] and MEAM potentials [35] are used for the description of Si-Si and Ni-Ni interactions, respectively. Interactions between Ni and Si atoms are described using Lennard-Jones (LJ) potentials [36].

For the LAMMPS-based simulations of *the re-structuring of the obtained thin Ni-film*, a wider Si structure with a surface area of 8.15 nm × 8.15 nm and with a reduced thickness of 1.69 nm is chosen, to avoid the cell size effect and shorten the simulation time [37]. The Ni thin film, with a thickness in the range of 0.3-1.2 nm, is annealed at temperatures of 600 K, 800 K, 1000 K and 1200 K. Ni-Ni, Si-Si and Ni-Si interactions are described using the Tersoff [34], MEAM [35] and LJ potentials [36], respectively. Note that the LJ pair potential does not allow to correctly describe physical / chemical processes such as Ni-atom diffusion into the Si substrate or the formation of Ni-silicide [38-40]. Therefore, to avoid an unphysical

diffusion of Ni atoms and an evaporation of Si atoms at high temperatures, the substrate atoms are immobilized during the simulation.

Combined molecular dynamics / time-stamped force-bias Monte Carlo (MD/tfMC) simulations are used for simulation of *the catalyzed CNT growth and hydrogenation/etching processes* [41-43]. In tfMC calculations, all the atoms in the system are displaced at once in every time step with unit probability, and thus generate a system evolution in a MD-like fashion. This technique can therefore very efficiently be coupled to canonical MD simulations [41]. Both during the MD and the tfMC cycles, ReaxFF is applied to describe the bond dissociation and formation processes, i.e., the C-C bond dissociation, dehydrogenation, rehydrogenation and H_2 formation, as well as other reactions [44, 45]. During the simulations, the Ni_{55} nanocatalyst is physisorbed on a virtual Al or Si substrate, employing a *z*-integrated Lennard-Jones potential [46]. Subsequently, the plasma-generated carbon precursor (C, C_2, C_2H, CH_3, CH_4, C_2H_2, C_6H_6, C_7H_8, and C_8H_{10}) is allowed to impinge on the cluster and its total density is kept constant in the gas-phase. In the case of CNT etching, also H-radicals are allowed to impinge on the tube wall. While these plasma species can have a wide energy range from thermal to hyperthermal [47], we choose thermal hydrocarbon species and H-radicals as plasma species in the simulations. When a gas-phase particle adsorbs on the nanocluster (or the nanotube), the resulting structure is allowed to relax by application of tfMC [41, 43]. During the relaxation, no new plasma species are allowed to impinge on the structure. All simulations are performed at a temperature in the range of 1000 K - 2000 K controlled by the canonical Bussi thermostat [48].

Finally, in order to clarify the role of H_2-plasma on the annealing of Ni-catalyst clusters, *the interactions of two Ni nanoclusters* are simulated using the combined reactive MD and tfMC technique in two regimes: (1) annealing without H_2 plasma and (2) annealing with H_2 plasma. In the simulations, Ni-Ni and Ni-H interactions are described using the ReaxFF potential, as parametrized by Mueller et al. [44, 45]. Prior to the annealing, two adjacent Ni_{55} nanoclusters are initially positioned at least 1 nm from each other. Both nanoclusters are physisorbed on a virtual Si substrate, employing a z-integrated Lennard-Jones potential [46]. Structures in both regimes are thermalized between 300 K and 800 K using the canonical Bussi thermostat [48].

2. Experimental procedure

The detailed description of the PECVD reactor and the growth of multi-wall CNTs (MWNTs) was reported in our previous studies [49, 50]. In these experimental studies, the growth of MWNTs is achieved on a Si substrate using Ni nanocatalyst by PECVD in three steps. In the first step, a 10 nm thin film of Ni is deposited onto the substrate by using a precision etching and coating system (PECS). Afterwards, the sample is transferred into the PECVD reactor (radio frequency capacitively coupled plasma (RF CCP) working at 13.56 MHz) and mounted on the grounded electrode. The 2nd step started once the base pressure inside the reactor is below $4 \cdot 10^{-4}$ Pa. In this step annealing with and without RF CCP treatment of the catalyst thin film is done at 923 K with a ramp time of 1200 s in a reducing atmosphere of hydrogen (10 sccm) at a pressure of 0.25 mbar and maintaining these conditions for 600 s. During 2nd step, the electrode distance is of about 2cm. In the 3rd step, the H_2 flow was increased to 40 sccm, the growth precursor C_2H_4 (20 sccm) is introduced, the pressure is increased up to 1 mbar, electrode distance was increased to 6 cm, and growth of CNTs is performed during 1800 s.

Results and discussion

1. Ni nanocluster formation

1.1 Deposition of Ni thin film. While Ni deposition has been experimentally studied [13, 40, 51], atomic-scale simulation results can provide details at the nanoscale of intermediate processes.

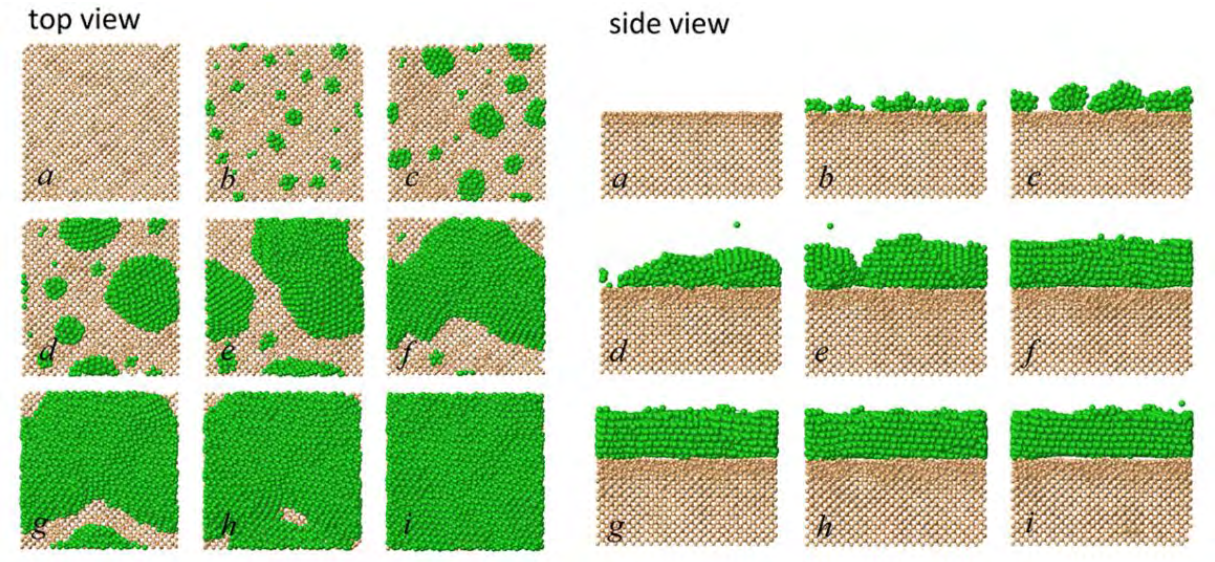

Figure 1 Snapshots of top and side views of the simulation cell during deposition of Ni atoms (green) on the Si(100) substrate (brown) at room temperature.

In the initial stage, incoming Ni atoms weakly adsorb on the Si surface, freely move over the surface and eventually find other Ni adatoms to form a small Ni cluster (Fig.1*b*), in agreement with experimental evidence [52]. During the deposition process, small clusters quickly sinter due to the weak interaction between the Ni-cluster and the Si surface (Fig.1*c*) [51]. As time advances, large clusters and subsequently islands gradually appear on the substrate (Fig.1*d-h*) before Ni completely covers the whole Si surface as a thin film (Fig.1*i*). The simulations thus show Ni-thin film growth through the Volmer–Weber (island) growth mode [53]. The obtained Ni film (with a thickness about 1.2 nm in Fig. 1*i*) is amorphous and the surface roughness is low, in agreement with experimental observations [13, 51].

1.2 Re-structuring of Ni thin film. After the deposition process, the obtained Ni thin film is annealed in order to obtain Ni nanoclusters on the Si surface (see Fig. 2, 0 ps, 1000 K and 1200 K).

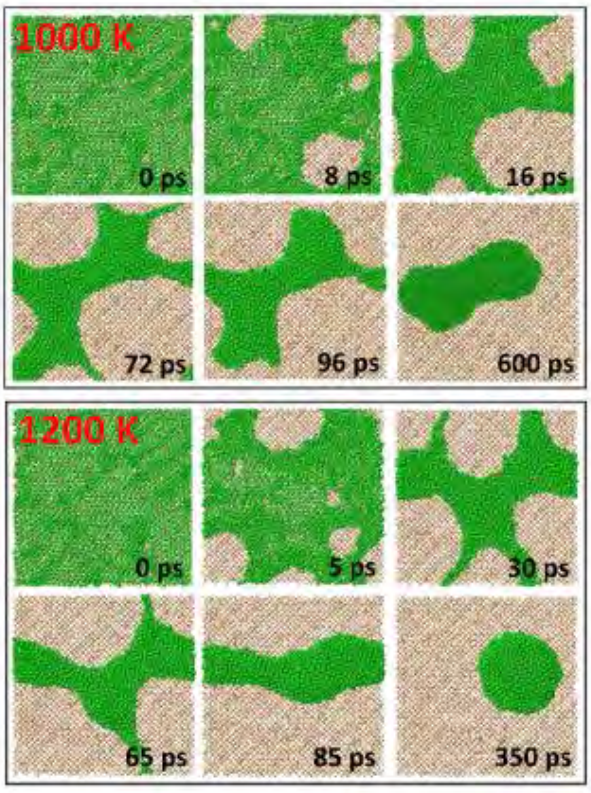

Figure 2 Evolution of the restructuring of a Ni film to the Ni nanocluster (or nanocatalyst) at temperatures of 1000 K and 1200 K during the annealing.

In Fig. 2, snapshots during the restructuring of the Ni film with thickness of 0.3 nm at a temperature of 1000 K and 1200 K are shown. When the annealing begins, the Ni thin film breaks due to its dewetting [37, 54, 55] and vacant holes start to appear on the Si surface after 8 ps and 5 ps at 1000 K and 1200 K, respectively. The area of the bare Si surface subsequently expands (see Fig. 2, 16 ps - 72 ps at 1000 K and 30 ps - 65 ps at 1200 K) and vacant holes coalesce (see Fig. 2, 96 ps and 85 ps at 1000 K and 1200 K, respectively). Subsequently, the Ni thin film eventually converts to a Ni nanocluster (Fig. 2, last panels for both temperatures). The snapshots demonstrate that the dewetting process strongly depends on the annealing temperature and the thickness of the Ni thin film, as well as the adhesion of the film-surface interface, which is in qualitative agreement with experimental observations [13, 56].

Due to the Gibbs-Tomson effect, i.e., the melting temperature depression in nanoscale systems [57, 58], the physical state of small cylindrical structures (indicated by the arrow in Fig. 3) changes (i.e., its fluidity increases). During the dewetting process, such small structures break up or collapse easily (Fig.3, cf. 72 ps and 78 ps) due to the capillary effect, which can be explained by the Plateau-Rayleigh instability [37, 59, 60]. According to this theory, the cylindrical fluid breaks up when its length (l) satisfies the condition $l > 2\pi r$, where r is the radius of the cylindrical fluid. In our case, the radius and length of the small cylindrical (fluid-like) structure shown in Fig. 3 (72 ps, indicated by the arrow) are approximately 0.3 nm and 3.6 nm, respectively, and the break up condition is thus satisfied.

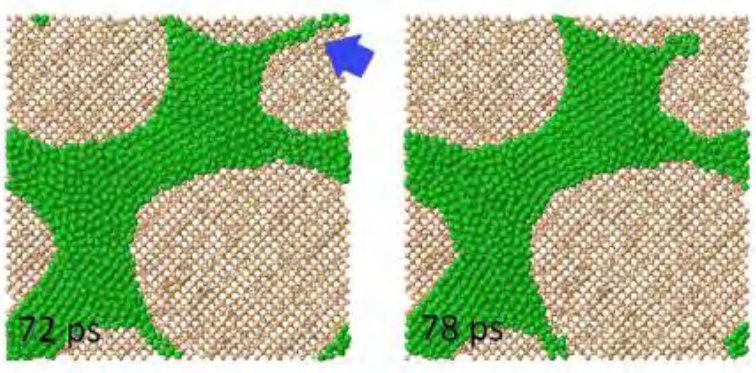

Figure 3 Breaking of a cylindrical Ni structure (indicated by the arrow) during the Ni re-structuring process at 1000K.

Indeed, the Plateau-Rayleigh instability explains the breakup of small structures observed in the simulations (see e.g. Fig. 3, 78 ps). Furthermore, our simulations reveal that the breakup speed depends on the surface temperature and inversely depends on the film-surface adhesion.

In our experiments, both small and large Ni clusters as well as Ni islands appear on the surface during the restructuring process (compare Fig. 2 and Fig. 4a). The number of larger clusters is seen to increase and the small clusters are seen to simultaneously disappear during the annealing process, which can be explained by Ostwald ripening [61]. According to this theory, the small clusters dissolve due to the minimization of the surface energy and their powders (or nanoclusters) redeposit onto the large cluster, which is energetically (thermodynamically) favored over the small clusters [62]. Consequently, only small and large clusters remain on the surface due to fast incorporation of the kinetically favored powders (nanoclusters), as shown in Fig. 4*a*. Indeed, the Ostwald ripening explains well these processes [63]. However, this theory fails to explain the remaining nanoclusters in the case of annealing with H_2 plasma as shown in Fig. 4*b*.

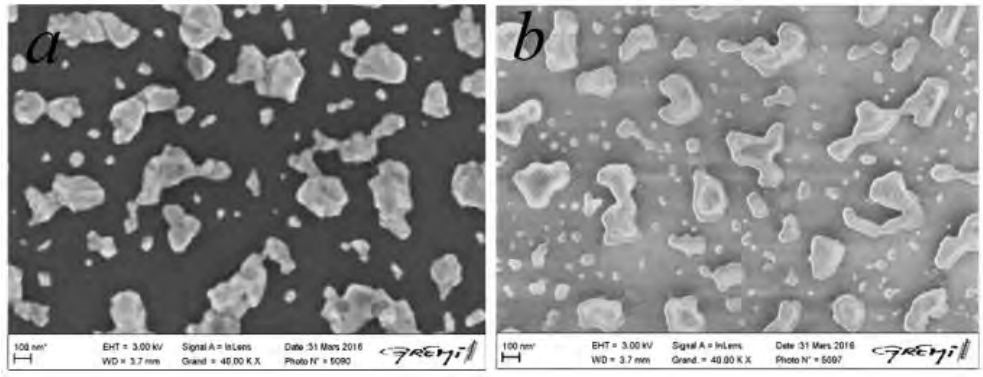

Figure 4 SEM images after the annealing of Ni film (white) with initial thickness of 6 nm on Si|SiO_2 substrate (black) at 650°C, (*a*) without and (*b*) with applying a H_2-plasma.

To understand this phenomenon, MD/tfMC simulations were performed, taking the following two observations into account: (i) the concentration of H radicals in a H_2 plasma is significantly higher than their concentration in TCVD [47, 64], and (ii) reactive H radicals/atoms bind strongly with Ni atoms and therefore nickel hydride is stable at low temperatures [65].

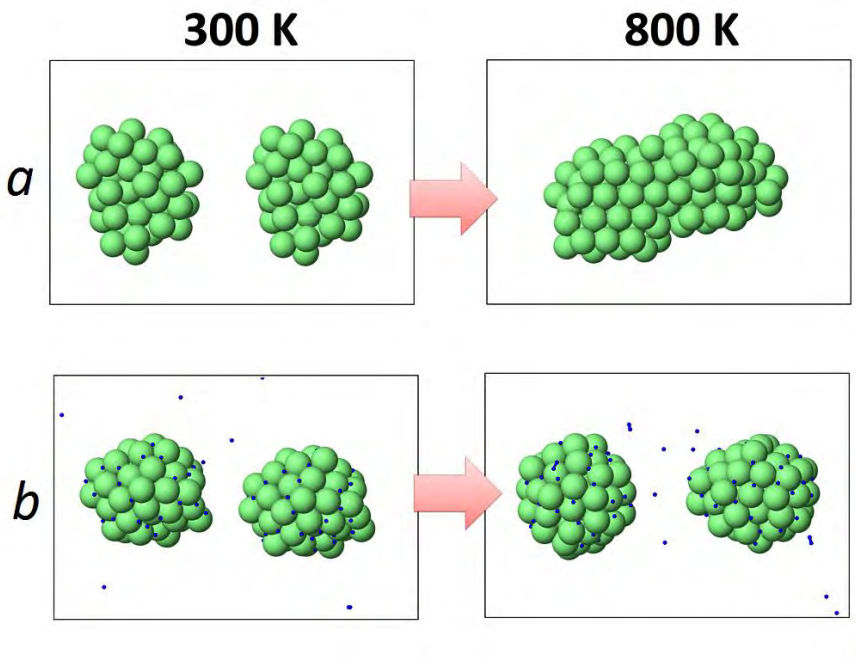

Figure 5 Top views of the interaction of two Ni_{55} nanoparticles on a virtual Si surface at temperatures of 300 K and 800 K in the regimes of annealing, (a) without and (b) with H_2-plasma. Here, Ni and H atoms are shown in green and blue colors, respectively.

In the simulations, H atoms are added to the gas phase and their number is kept constant during the annealing in the plasma case (Fig. 5*b*). Furthermore, hydrogenated Ni_{55} (*h*-Ni) nanoclusters are used in the annealing process, in agreement with the second observation. Structures in both regimes are thermalized at a temperature from 300 K up to 800 K. At the end of the annealing process, the nanoclusters coalesce in the first (thermal) regime (Fig. 5*a*), while the *h*-Ni nanoclusters do not sinter on the surface in the second (plasma) regime. In the annealing-only regime, the clusters are connected through surface Ni atoms, which have dangling bonds. Such bonds, however, are terminated by reactive H atoms (radicals) in the "annealing + plasma" regime even at low temperature (Fig. 5*b*). As a result, the interaction between adjacent Ni hydride nanoclusters becomes very weak and they cannot sinter. The results show that at low temperature (300 K), the nanoclusters do not sinter/coalesce, regardless of the presence or absence of H_2, due to their low mobility and weak mutual interaction. At high temperature (800 K), however, the coalescence depends on the presence of H_2, as at this temperature their mobility is much higher. Note also that when the temperature continues to increase, the sintering speed gradually enhances due to the temperature-dependent H_2 desorption and consequently the removal of the hydrogen shell from these nanoclusters.

In general, the obtained results indicate that the Ostwald ripening discontinues or retards due to the H-effect in the second regime. Due to this effect, Ni nanoparticles (powders) can remain stable for a longer time on the surface in the plasma regime. Indeed, the obtained results allow us a better understanding the difference of the re-structuring nature of Ni thin film in the annealing with H_2 plasma. Finally, the obtained Ni-nanoclusters are used as a catalyst in our simulations for the CNT nucleation from plasma species.

2. CNT nucleation and etching

2.1 CNT nucleation from plasma-generated species. From the simulations, we distinguish three main stages in the catalyzed nucleation of carbon nanotubes from hydrocarbon C_nH_m plasma species: (i) incubation, (ii) cap formation and (iii) continued tube growth. Also, these stages are discussed in our previous work, devoted to the CNT nucleation from hydrocarbon molecules in a TCVD setup [28].

In the beginning of stage I, gas-phase hydrocarbon species impinge on the cluster and they gradually dissociate by virtue of the Ni nanocatalyst. Subsequently, free H-adatoms move around the nanocluster surface and find another H-adatom, resulting in H_2 desorption. The remaining C adatoms subsequently dissolve into the Ni cluster. This "C_nH_m adsorption/dissociation, C dissolution and H_2 desorption" scenario continues until the nanocluster is saturated (Fig. 6a, frame 1). Subsequently, segregated C-atoms diffuse over and through the catalyst (sub)surface until recombining with other carbon atom(s) in order to form initial surface carbon structures, i.e., C_2 dimers, sp^2 and sp^3 C atoms and short C_y polyyne chains without or with H-terminations (Fig. 6a, frame 2).

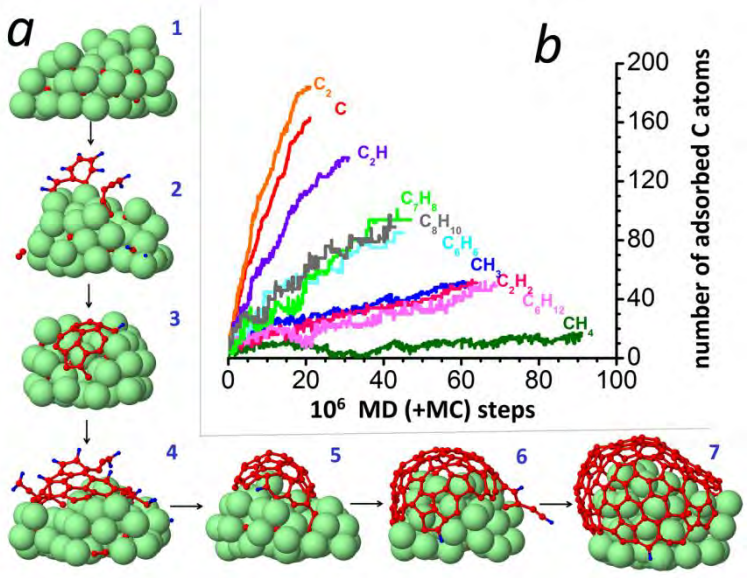

Figure 6 (*a*) Nucleation process of a CNT from C_nH_m species on a Ni nanocatalyst, which is physisorbed on a virtual Al or Si substrate. Here, Ni, C and H atoms are in green, red and blue colors, respectively; (*b*) evolution of adsorbed C atoms on/in the Ni nanocluster during the CNT nucleation from different hydrocarbon species. For the sake of clarity, the different cases are presented in different colors.

When rehydrogenation occurs, the surface carbon structures, including polyyne chains and the graphene-like network (Fig. 6a, frame 3) become partially hydrogenated and vertically freestanding graphene sheets can be formed on the catalyst surface (Fig. 6a, frame 4). Due to competition between dehydrogenation and rehydrogenation, both horizontally and vertically oriented carbon patches can be found on the Ni surface (cf. Fig. 6a, frames 3 and 4) [46]. The results show that this competition depends on the growth temperature, type of hydrocarbon species and their gas-phase pressure (or flux), as well as the catalyst-surface adhesion [28]. Such competition can explain the appearance of unstable carbon structures in the incubation stage of CNT growth, as observed in the *in-situ* transmission electron microscopy (TEM) observations by Yoshida *et al*. [66]. As time advances, the vertical free-standing networks invariably and irreversibly transform to horizontal networks covering the surface. Also, we found in previous investigations that such vertical carbon networks can remain stable on the surface, and they stack up parallel at low temperatures [28, 46]. The appearance of such structures could also explain the onset of MWNT formation [28], as suggested earlier by Hoffman *et al*. [67]. At the end of the first growth stage, the graphitic network(s) start(s) to gradually cover the nanocluster surface.

The second stage of the CNT nucleation is characterized by the appearance of a carbon cap on the cluster (Fig. 6a, frame 5), which is essential for the nucleation of a CNT. The simulation results confirm our previous conclusions that cap nucleation in CNT growth from hydrocarbon species does not require the formation of long polyyne chains [68], which is in contrast to the many simulations using hydrogen-free carbon as growth precursor [28].

In the third stage, the carbon nanotube continues to grow on the catalyst surface (Fig. 6a, frames 6 and 7) due to the incorporation of the segregated C atoms, diffusing C adatoms or through direct adsorption of partially dehydrogenated $C_{n-x}H_{m-y}$ fragments near the catalyst/cap interface followed by dehydrogenation. Overall, two scenarios turn out to be possible after the saturation sub-stage: (1) either C atoms continue to diffuse into the cluster, provided they completely lose their hydrogens, or (2) they diffuse over the catalyst surface, in case they

keep or only partially lose their hydrogen. In either case, the C-atoms eventually incorporate into the growing network [28].

Also, our simulations show that the C adsorption/incorporation rate during the CNT nucleation depends on the number of C and H atoms as well as the H/C ratio in each plasma species (Fig 6b). Specifically, if the ratio tends to zero, the number of system C atoms rises faster, i.e., the adsorption rate of C atoms increases in the following order for the precursors: $CH_4 \rightarrow CH_3 \rightarrow C$ or $C_2H_2 \rightarrow C_2H \rightarrow C_2$. In the case where the H/C ratio is (nearly) equal for two different precursors, the adsorption rate depends on the number of C atoms in the precursor (Fig. 6b, cf. C_2H_2 and C_6H_6). Indeed, the C-addition rate decreases and consequently the C adsorption/incorporation can be delayed, if the hydrogen concentration increases in the system. Due to this effect, the CNT nucleation slows down and the grown structures can additionally be damaged in the plasma-assisted CNT growth [10, 29]. Note also that μm-length CNTs can catalyze some carbon nanostructures, including carbon nanowalls, when the concentration of C radicals exceeds that in the plasma environment [69, 70]. However, no experimental observation of this phenomenon in the CNT nucleation stage has been reported.

2.2 Plasma-assisted etching of carbon nanotubes. Our simulations show that the incipient or small carbon nanotubes during their plasma-assisted growth can be eventually removed from the catalyst surface, if the plasma contains a high concentration of H-radicals. Fig.7a shows that the ideal nanotube (frame 1) is gradually damaged and etched (frames 2-8) before its total elimination (frame 9) upon hydrogenation. Incoming H-atoms preferable stick on the catalyst particle, as well as on the top of the tube (Fig. 7a, frame 2) due to its relatively high curvature. The latter is explained by the increased reactivity due to the increase of the pyramidalization and misalignment of the π-orbitals of the C-atoms of the tube cap [71]. According to our previous calculations, the energy barrier for H-diffusion (0.57 eV) on the Ni-catalyst surface is about three times lower than the barrier for H_2-formation and desorption (1.63 eV) [72, 73]. Therefore, H-adatoms can easily move on the tube wall before they either locally associate (i.e., H-clustering effect [74]) or desorb as H_2-molecules, according to the Langmuir–Hinshelwood (LH) recombinative desorption or the Eley–Rideal (ER) abstraction mechanisms [75-77]. As a result, the nanotube surface is not fully covered by a “hydrogen shell” and the coverage does not reach one-third of the surface [73] due to simultaneous dehydrogenation. At the same time, the tube surface is locally amorphized and the tube curvature is locally increased due to the H-coalescence [74]. In this amorphized and high-

curvature site of the tube, three different H-pairs, i.e., para, ortho and meta pairs can be found. Among them, in particular the ortho H pairs seriously affect the carbon network. Specifically, they significantly elongate the C-C bond length which eventually leads to the initiation of the etching process (Fig.7a, frame 3). Recently, we found that the onset of selective CNT etching also depends on the angle between the HC-CH bond and the tube chirality vector, in addition to the tube metallicity and curvature [73].

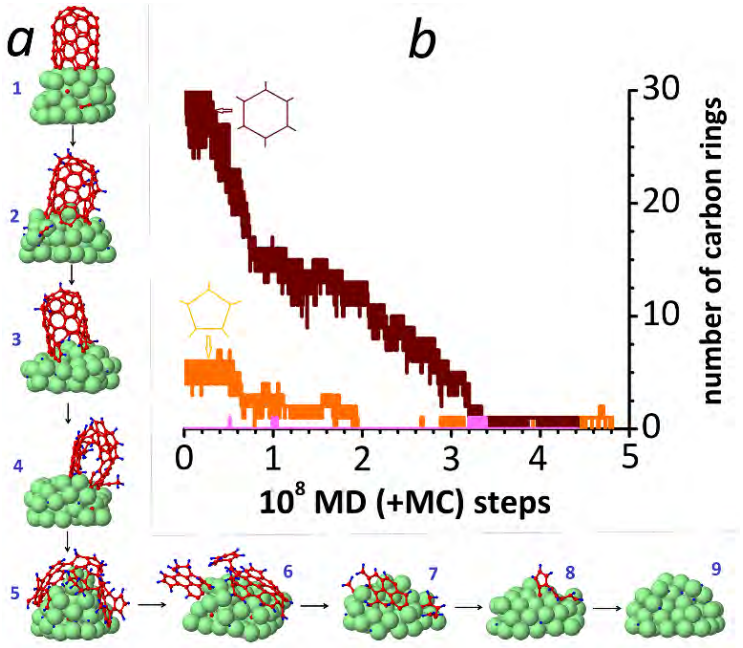

Figure 7 (*a*) Hydrogenation and etching process for a base-grown (5,5) tube; and (*b*) number of carbon rings (hexagon, pentagon, etc) as a function of the number of MD(+MC) steps.

After the first C-C bond breaking, the etching area propagates around this defected site due to fast H-occupation. Also, adsorbed H atoms have the tendency to move and cluster on the opposite part of the defected tube and begin the etching at that site as well (Fig.7a, frame 4). Such etching behavior leads to the formation of parallel nanotube ribbons, which has already been experimentally observed [78]. The defected tube finally collapses and partially covers the cluster surface (Fig.7a, frame 5). In this tube/sheet transition, the removal rate of hexagon rings in the carbon network significantly decreases, as shown in Fig. 7b (after $0.7 \cdot 10^8$ MD(+MC) steps). Also, the number of pentagon rings considerably decreases. This clearly indicates that the obtained nanosheet becomes a nearly perfect C network due to the etching or catalyst-assisted conversion of pentagons, heptagons, and other C rings into hexagons. Such conversion eventually allows the appearance of graphene patches on the cluster [46].

Due to hydrogenation or rehydrogenation, their edges are partially terminated by H atoms and thus free-standing graphene patches or graphene nanowalls can form on the catalyst surface (Fig.7a, frame 6). The formation of such nanowalls is also in agreement with experimental evidence that no carbon nanowalls are formed without H_2 gas flow or without irradiation by H radicals [79]. Subsequently, sheet/wall or wall/sheet transformations occur, due to the competition between (re)hydrogenation and dehydrogenation as well as H-etching. As mentioned in the previous section, such unstable carbon structures were also detected during *in situ* TEM observations before the CNT nucleation from C_2H_2 [66]. The size of these unstable nanostructures continuously decreases during the hydrogenation/etching process (Fig.7a, frame 7). Finally, we can find ordinary carbon structures, i.e., simple carbon rings and carbon polyyne chains on the catalyst surface (Fig.7a, frame 8) before the complete removal of the CNT. Note that while increasing flow of hydrogen can speed up the degradation/etching process, it does not change the etching scenario.

During the entire hydrogenation and subsequent etching process, the number of H adatoms first increases until the etching onset and their number gradually reduces afterwards due to both the H_2 formation and the etching, while the surface C atoms are continuously removed. Finally, we observed mostly methane and ethylene molecules, as well as methyl radicals besides other etched hydrocarbon species in the gas phase, in addition to a high number of H radicals and H_2 molecules during the hydrogenation and subsequent etching process.

Conclusion

We study the nanoscale mechanisms for the Ni-catalyzed CNT growth in a hydrogen-containing plasma environment using our hybrid MD/MC simulation technique and TEM-based experiments.

We conclude that the role of hydrogen in the re-structuring of a Ni film and consequent appearance of Ni nanoclusters, as well as in the CNT nucleation/etching from plasma species, is very important and thus its careful control during aforementioned processes is essential. Specifically, the H_2 plasma can delay the sintering of the Ni powders and this leads to maintain nanoparticles longer on the semiconductor surface. Also, in CNT nucleation, the C adsorption rate is found to inversely depend on the H content in the plasma precursor. Moreover, due to the H-effect, i.e., hydrogenation, dehydrogenation and H-etching, different C structures, including nanosheets, nanowalls, and free-standing polyyne chains can be found

during both CNT nucleation and etching processes. All obtained results are in agreement with available literature data, including theoretical and experimental evidences.

In general, this study clarifies the nanoscale mechanisms in the nanocatalyst formation and subsequent carbon nanotube nucleation/etching in a plasma environment which is important for the eventual goal of understanding the selective synthesis of CNTs with a definable chirality.

Acknowledgments

U. K. gratefully acknowledges financial support from the Fund of Scientific Research Flanders (FWO), Belgium (Grant No. 12M1315N). The work was carried out in part using the Turing HPC infrastructure of the CalcUA core facility of the Universiteit Antwerpen, a division of the Flemish Supercomputer Centre VSC, funded by the Hercules Foundation, the Flemish Government (department EWI) and the Universiteit Antwerpen. The authors also thank Prof. A. C. T. van Duin for sharing the ReaxFF code.

References

1. S. Iijima, Helical microtubules of graphitic carbon. *Nature* 1991, 354, 56-58.
2. S. Iijima, T. Ichihashi, Single-shell carbon nanotubes of 1-nm diameter. *Nature* 1993, 363, 603-605.
3. D. S. Bethune, C. H. Kiang, M. S. de Vries, G. Gorman, R. Savoy, J. Vazquez, R. Beyers, Cobalt-catalysed growth of carbon nanotubes with single-atomic-layer walls. *Nature* 1993, 363, 605-607.
4. R. H. Baughman, A. A. Zakhidov, W. A. de Heer, Carbon Nanotubes-the Route Toward Applications. *Science* 2002, 297, 787-792.
5. J.-P. Tessonnier, D. S. Su, Recent Progress on the Growth Mechanism of Carbon Nanotubes: A Review. *ChemSuSChem* 2011, **4**, 824-847.
6. V. Jourdain, C. Bichara, Current understanding of the growth of carbon nanotubes in catalytic chemical vapour deposition. *Carbon* 2013, **58**, 2-39.
7. E. C. Neyts, PECVD growth of carbon nanotubes: From experiment to simulation. *J. Vac. Sci. Technol. B* 2012, **30**, 030803.

8. A. Thess, R. Lee, P. Nikolaev, H. Dai, P. Petit, J. Robert, C. Xu, Y. H. Lee, S. G. Kim, A. G. Rinzler, D. T. Colbert, G. E. Scuseria, D. Tomanek, J. E. Fischer, R. E. Smalley, Crystalline Ropes of Metallic Carbon Nanotubes. *Science* 1996, 273, 483-487.
9. W. Z. Li, S. S. Xie, L. X. Qian, B. H. Chang, B. S. Zou, W. Y. Zhou, R. A. Zhao, G. Wang, Large-Scale Synthesisi of Aligned Carbon Nanotubes, *Science* 1996, 274, 1701-1703.
10. T. Kato and R. Hatakeyama, Growth of Single-Walled Carbon Nanotubes by Plasma CVD. *Journal of Nanotechnology* 2010, **2010**, 1-11.
11. R. Hatakeyama, T. Kaneko, T. Kato, Y. F. Li, Plasma-synthesized single-walled carbon nanotubes and their applications. *J. Phys. D: Appl. Phys.* 44 (2011) 174004.
12. Ghorannevis, Z.; Kato, T.; Kaneko, T.; Hatakeyama, R. Narrow-Chirality Distributed Single-Walled Carbon Nanotube Growth from Nonmagnetic Catalyst. *J. Am. Chem. Soc.* 132 (2010) 9570.
13. M. Cantoro, S. Hofmann, C. Mattevi, S. Pisana, A. Parvez, A. Fasoli, C. Ducati, V. Scardaci, A. C. Ferrari, J. Robertson, Plasma restructuring of catalysts for chemical vapor deposition of carbon nanotubes. *J. Appl. Phys.* **105**, 064304 (2009).
14. S. Esconjauregui, B. C. Bayer, M. Fouquet, C. T. Wirth, C. Ducati, S. Hofmann, J. Robertson, Growth of high-density vertically aligned arrays of carbon nanotubes by plasma-assisted catalyst pretreatment. *Appl. Phys. Lett.* **95**, 173115 (2009).
15. J. Robertson, S. Hofmann, M. Cantaro, A. Parvez, C. Ducati, G. Zhong, R. Sharma, and C. Mattevi, Controlling the Catalyst During Carbon Nanotube Growth. *J. Nanosci. Nanotechnol.* **8**, 1−7 (2008).
16. Amara, H., Roussel, J. -M., Bichara, C., Gaspard, J.-P. & Ducastelle, F. A tight-binding potential for atomistic simulations of carbon interacting with transition metals: Application to the Ni-C system. *Phys. Rev. B* **79,** 014109 (2009).
17. Amara, H., Bichara, C. & Ducastelle, F. Understanding the nucleation mechanisms of carbon nanotubes in catalytic chemical vapor deposition. *Phys. Rev. Lett*. **100,** 056105 (2008).
18. Gómez-Gualdrón, D. A. & Balbuena, P. B. Characterization of carbon atomistic pathways during single-walled carbon nanotube growth on supported metal nanoparticles. *Carbon* **57,** 298–309 (2013).
19. Ohta, Y., Okamoto, Y., Irle S. & Morokuma, K. Rapid Growth of a Single-Walled Carbon Nanotube on an Iron Cluster: Density-Functional Tight-Binding Molecular Dynamics Simulations**.** *ACS Nano* **2**, 1437–1444 (2008).

20. Page, A. J., Yamane, H., Ohta, Y., Irle, S. & Morokuma, K. QM/MD Simulation of SWNT Nucleation on Transition-Metal Carbide Nanoparticles. *J. Am. Chem. Soc.* **132,** 15699–15707 (2010).
21. Börjesson, A. & Bolton, K. First Principles Studies of the Effect of Nickel Carbide Catalyst Composition on Carbon Nanotube Growth. *J. Phys. Chem. C* **114,** 18045–18050 (2010).
22. Diarra, M., Amara, H., Bichara, C. & Ducastelle, F. Role of defect healing on the chirality of single-wall carbon nanotubes. *Phys. Rev. B*. **85,** 245446 (2012).
23. Neyts, E. C., van Duin A. C. T. & Bogaerts, A. Changing Chirality during Single-Walled Carbon Nanotube Growth: A Reactive Molecular Dynamics/Monte Carlo Study. *J. Am. Chem. Soc*. **133,** 17225–17231 (2011).
24. Gómez-Gualdrón, D. A., Beetge, J. M., Burgos, J. C. & Balbuena, P. B. Effects of Precursor Type on the CVD Growth of Single-Walled Carbon Nanotubes. *J. Phys. Chem. C* **117,** 10397–10409 (2013).
25. Shariat, M., Hosseini, S. I., Shokri B. & Neyts, E. C. Plasma enhanced growth of single walled carbon nanotubes at low temperature: A reactive molecular dynamics simulation. *Carbon* **65,** 269–276 (2013).
26. M. Shariat, B. Shokri, E. C. Neyts, On the low-temperature growth mechanism of single walled carbon nanotubes in plasma enhanced chemical vapor deposition. *Chem. Phys. Lett*. 2013, **590**, 131.
27. Neyts, E. C., Ostrikov, K., Han, Z. J., Kumar, S., van Duin, A. C. T. & Bogaerts, A. Defect Healing and Enhanced Nucleation of Carbon Nanotubes by Low-Energy Ion Bombardment. *Phys. Rev. Lett*. **110**, 065501 (2013).
28. U. Khalilov, A. Bogaerts and E. C. Neyts, Atomic scale simulation of carbon nanotube nucleation from hydrocarbon precursors. *Nat. Commun*., 2015, **6**, 10306.
29. Zhang, G., Qi, P., Wang, X., Lu, Y., Li, X., Tu, R., Bangsaruntip, S., Mann, D., Zhang, L & Dai, H. Selective Etching of Metallic Carbon Nanotubes by Gas-Phase Reaction. *Science* **304**, 974 (2006).
30. T. Kato and R. Hatakeyama, Formation of Freestanding Single-Walled Carbon Nanotubes by Plasma-Enhanced CVD. *Chem. Vap. Deposition* 2006, **12**, 345.
31. S. Plimpton, Fast Parallel Algorithms for Short-Range Molecular Dynamics. *J. Comput. Phys*. **117**, 1-19 (1995).

32. H. J. C. Berendsen, J. P. M. Postma, W. F. van Gunsteren, A. DiNola, J. R. Haak, Molecular dynamics with coupling to an external bath. *J. Chem. Phys*. **81**, 3684-3690 (1984).
33. L. Xie, P. Brault, J.-M. Bauchire, A.-L. Thomann, L. Bedra, Molecular Dynamics simulations of clusters and thin film growth in the context of plasma sputtering deposition. *J. Phys. D* **47**, 224004 (2014).
34. J. Tersoff, New empirical approach for the structure and energy of covalent systems. *Phys. Rev. B* **37**, 6991 (1988).
35. M. I. Baskes, Modified embedded-atom potentials for cubic materials and impurities. *Phys. Rev. B* **46**, 2727-2742 (1992).
36. L. Xie, P. Brault, A.-L. Thomann, J.-M. Bauchire, AlCoCrCuFeNi high entropy alloy cluster growth and annealing on silicon: A classical molecular dynamics simulation study. *Applied Surface Science* 285P, 810– 816 (2013).
37. Y. Maekawa, Y. Shibuta, Dewetting dynamics of nickel thin film on alpha-quartz substrate: A molecular dynamics study. *Chem. Phys. Lett.* 658, 30-36 (2016)
38. A. Alberti, A. La Magna, Role of the early stages of Ni-Si interaction on the structural properties of the reaction products, *J. Appl. Phys*., 2013, 114, 121301.
39. A. M. Thron, P. K. Greene, K. Liu, K. van Benthem, Structural changes during the reaction of Ni thin films with (100) silicon substrates, *Acta Materialia* 60 (2012) 2668–2678.
40. V. V. Bakovets, V. N. Mitkin, N. V. Gelfond, Mechanism of Ni Film CVD with a $Ni(Ktfaa)_2$ precursor on a Silicon Substrate, *Chem. Vap. Deposition* 2005, 11, 368-374.
41. K. M. Bal, E. C. Neyts, On the time scale associated with Monte Carlo simulations. *J. Chem. Phys.* 2014, **141**, 204104.
42. E. C. Neyts, Y. Shibuta, A. C. T. van Duin, A. Bogaerts, Catalyzed Growth of Carbon Nanotube with Definable Chirality by Hybrid Molecular Dynamics Force Biased Monte Carlo Simulations. *ASC Nano* 2010, **4,** 6665-6672.
43. E. C. Neyts, B. J. Thijsse, M. J. Mees, K. M. Bal, G. Pourtois, Establishing Uniform Acceptance in Force Biased Monte Carlo Simulations. *J. Chem. Theory Comput*. **8**, 1865-1869 (2012).
44. A. C. T. van Duin, S. Dasgupta, F. Lorant, W. A. Goddard III, ReaxFF: A Reactive Force Field for Hydrocarbons. *J. Phys. Chem. A* **105,** 9396-9409 (2001).

45. J. E. Mueller, A.C.T. van Duin, W. A. Goddard III, Development and Validation of ReaxFF Reactive Force Field for Hydrocarbon Chemistry Catalyzed by Nickel. *J. Phys. Chem. C* 2010, **114,** 4939-4949.
46. U. Khalilov, A. Bogaerts, E. C. Neyts, Microscopic mechanisms of vertical graphene and carbon nanotube cap nucleation from hydrocarbon growth precursors. *Nanoscale* 2014, **6**, 9206-9214.
47. D. B. Hash, M. Meyyappan, Model based comparison of thermal and plasma chemical vapor deposition of carbon nanotubes. *Journal of Applied Physics* 2003, **93**, 750.
48. G. Bussi, D. Donadio, M. Parrinello, Canonical sampling through velocity-rescaling. *J. Chem. Phys*. 2007, **126,** 014101.
49. T. Labbaye, A. Canizares, M. Gaillard, T. Lecas, E. Kovacevic, C. Boulmer-Leborgne, T. Strunskus, N. Raimboux, P. Simon, G. Guimbretière, M.-R. Ammar, In situ Raman spectroscopy for growth monitoring of vertical aligned multiwall carbon nanotubes in plasma reactor. *Appl. Phys. Lett.* **105**, 213109 (2014).
50. M. Gaillard, C. Kübel, C. Boulmer-Leborgne, D. Wang, N. Semmar, A. Petit, E. Millon, High-resolution transmission electron microscope observations of multiwalled carbon nanotube microstructures grown by plasma enhanced chemical vapor deposition. *J. Vac. Sci. Technol. B*, 2013, **31**, 031805.
51. D. S. Ghosh, Ultrathin Metal Transparent Electrodes for the Optoelectronics Industry, *Chapter 2 Basics of Ultrathin Metal Films and Their Use as Transparent Electrodes*, 2013, Springer XII, p 86.
52. D. Niwa, T. Homma and T. Osaka, Deposition Mechanism of Ni on Si(100) Surfaces in Aqueous Alkaline Solution. *J. Phys. Chem. B* **108**, 9900-9904 (2004).
53. M. Volmer, A. Weber, Nucleus formation in supersaturated systems. *Z. Phys. Chem*. 119, 6274 (1926)
54. H. Krishna, N. Shirato, S. Yadavali, R. Sachan, J. Strader, R. Kalyanaraman, Self-Organization of Nanoscale Multilayer Liquid metal Films: Experiment and Theory. *ACS Nano* **5**, 470-476 (2011).
55. R. J. Peláez, T. Kuhn, C. E. Rodriguez, C. N. Afonso, Dynamics of laser induced metal nanoparticle and pattern formation. *Appl. Phys. Lett*. **106**, 061914 (2015).
56. S. Esconjauregui, S. Bhardwaj, J. Yang, C. Castellarin-Cudia, R. Xie, L. D'Arsié, T. Makaryan, H. Sugime, S. Eslava, C. Cepek, J. Robertson, *Carbon* **73**, 13-24 (2014).
57. Buffat, Ph. & Borel, J-P. Size effect on the melting temperature of gold particles. *Phys. Rev. A* **13**, 2287-2298 (1976)..

58. Shibuta, Y. & Suzuki, T. A molecular dynamics study of the phase transition in bcc metal nanoparticles. *J. Chem. Phys.* **129**, 144102 (2008).
59. J. Plateau, *Statique Experimentale et Theorique des Liquides Soumis aux Seules Forces Moleculaires*, 2, Gauthier-Villars, (1873).
60. L. Rayleigh, *Proc. London Math. Soc.***10**, 4 (1878).
61. W. Ostwald, *Lehrbuch der Allgemeinen Chemie*, vol. 2, part 1. Leipzig, Germany (1896).
62. P. W. Voorhees, The Theory of Ostwald Ripening, *J. Stat Phys*. **38**, 231-252 (1985).
63. T. W. Hansen, A. T. DeLariva, A. R. Challa, A. K. Datye, Sintering of Catalytic Nanoparticles: Particle Migration or Ostwald Ripening? *Acc. Chem. Res*., 2012, doi: 10.102/ar3002427.
64. M. J. Behr, E. A. Gaulding, K. A. Mkhoyan, E. S. Aydil, Hydrogen etching and cutting of multiwall carbon nanotubes. *J. Vac. Sci. Technol.* B 2010, **28**, 1187.
65. J. E. Mueller, A. C. T. van Duin and W. A. Goddard III, Structures, Energetics, and Reaction for CH_x Bound to the nickel (111) Surface. *J. Phys. Chem. C* **113**, 20290-20306 (2009).
66. H. Yoshida, S. Takeda, T. Uchiyama, H. Kohno and Y. Homma, Atomic-Scale In-situ Observation of Carbon Nanotube Growth from Solid State Iron Carbide Nanoparticles. *Nano Lett.* 2008, **8,** 2082-2086.
67. S. Hofmann, R. Sharma, C. Ducati, G. Du, C. Mattevi, C. Cepek, M. Cantaro, S. Pisana, A. Parvez, F. Cervantes-Sodi, A. C. Ferrari, R. Dunin-Borkowski, S. Lizzit, L. Petaccia, A. Goldoni, J. Robertson, In situ Observations of Catalyst Dynamics during Surface-Bound Carbon Nanotube Nucleation. *Nano Lett.* 2007, **7**, 602-608.
68. A. J. Page, F. Ding, S. Irle, K. Morokuma, Insights into carbon nanotube and graphene formation mechanisms from molecular simulations: a review. *Rep. Prog. Phys*. 2015, **78**, 036501.
69. A. Malesevic, S. Vizireanu, R. Kemps, A. Vanhulsel, C. Van Haesendonck, G. Dinescu, Combined growth of carbon nanotubes and carbon nanowalls by plasma-enhanced chemical vapor deposition. *Carbon* 2007, **45**, 2932.
70. R. E. Morjan, V. Maltsev, O. Nerushev, Y. Yao, L. K. L. Falk, E. E. B. Campbell, High growth rates and wall decoration of carbon nanotubes grown by plasma-enhanced chemical vapor deposition. *Chemical Physics Letters* 2004, **383**, 385.
71. S. Niyogi, M. A. Hamon, H. Hu, B. Zhao, P. Bhowmik, R. Sen, M. E. Itkis, R. C. Haddon, Chemistry of Single-Walled carbon Nanotubes. *Acc. Chem. Res.* **35**, 1105-1113 (2002).

72. W. Somers, A. Bogaerts, A. C. T. van Duin, S. Huygh, K. M. Bal, E. C. Neyts, Temperature influence on the reactivity of plasma species on a nickel catalyst surface: An atomic scale study. *Catal. Today* **211,** 131-136 (2013).
73. U. Khalilov, A. Bogaerts, Y. Xu, T. Kato, T. Kaneko, E. C. Neyts, How the alignment of adsorbed ortho H pairs determines the onset of selective carbon nanotube etching. *Nanoscale* **9**, 1653-1661 (2017).
74. W. Andreoni, A. Curioni, J. M. H. Kroes, F. Pietrucci, O. Gronin, Exohedral Hydrogen Chemisorption on a Carbon Nanotube: The Clustering Effect. *J. Phys. Chem. C* 2012, **116**, 269–275.
75. X. Sha, B. Jackson, D. Lemoine, Quantum studies of Eley-Rideal reactions between H atoms on a graphite surface. *J. Chem. Phys.* 2002, **116**, 7158.
76. T. Zecho, A. Güttler, X. Sha, D. Lemoine, B. Jackson, J. Küppers, Abstraction of D chemisorbed on graphite (0001) with gaseous H atoms. *Chem. Phys. Lett.* 2002, **366**, 188-195.
77. E. Neyts, Plasma-Surface Interactions in Plasma Catalysis, *Plasma Chem. Plasma Process* 2016, **36**, 185-212.
78. N. G, Chopra, L. X. Benedict, V. H. Crespi, M. L. Cohen, S. G. Louie & A. Zettl, Fully collapsed carbon nanotubes. *Nature* 1995, **377**, 135.
79. H. Kondo, M. Hori and M. Hiramatsu (**2011**). Nucleation and Vertical Growth of Nano Graphene Sheets, Graphene - Synthesis, Characterization, Properties and Applications, Prof. Jian Gong (Ed.), ISBN: 978-953-307-292-0, InTech, Available from: http://www.intechopen.com/books/graphene-synthesischaracterization-properties-and-applications/nucleation-and-vertical-growth-of-nano-graphene-sheets